
This is an electronic reprint of the original article.
This reprint may differ from the original in pagination and typographic detail.

Mousapour, Mehrdad; Partanen, Jouni; Salmi, Mika

NiTiCu alloy from elemental and alloyed powders using vat photopolymerization additive manufacturing

Published in:
Additive Manufacturing

DOI:
[10.1016/j.addma.2023.103853](https://doi.org/10.1016/j.addma.2023.103853)

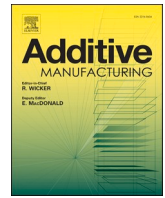
Published: 25/09/2023

Document Version
Publisher's PDF, also known as Version of record

Published under the following license:
CC BY

Please cite the original version:
Mousapour, M., Partanen, J., & Salmi, M. (2023). NiTiCu alloy from elemental and alloyed powders using vat photopolymerization additive manufacturing. *Additive Manufacturing*, 78, Article 103853.
<https://doi.org/10.1016/j.addma.2023.103853>

This material is protected by copyright and other intellectual property rights, and duplication or sale of all or part of any of the repository collections is not permitted, except that material may be duplicated by you for your research use or educational purposes in electronic or print form. You must obtain permission for any other use. Electronic or print copies may not be offered, whether for sale or otherwise to anyone who is not an authorised user.



NiTiCu alloy from elemental and alloyed powders using vat photopolymerization additive manufacturing

Mehrdad Mousapour^{*}, Jouni Partanen, Mika Salmi

Department of Mechanical Engineering, Aalto University, Puumiehenkuja 3, 02150 Espoo, Finland

ARTICLE INFO

Keywords:

Additive manufacturing (AM)
Stereolithography
Elemental powder
Mechanical alloying
NiTi-based alloys

ABSTRACT

The metal vat photopolymerization technique (MVP) has high potential for metal part production because of its high accuracy, speed, and flexibility. However, low density, poor mechanical properties, and effects of sintering parameters on the properties are some of the challenges in MVP. This paper is the first to investigate the possibility of producing a NiTiCu metal alloy using VP from Ni, Ti, and Cu elemental and mechanically alloyed powders. The effect of particle size distribution and solid content on the physical and mechanical properties is also studied and compared. The results indicate that all three elements are homogeneously distributed in the whole print without premixing the powders, which considerably reduces processing time. Finer particle size and higher solid content also improve densification degree, hardness, flexural strength, and surface quality of the final parts. The measured surface roughness (R_a) of NiTiCu was 6.42 μm and 10.31 μm for milled and elemental powders, respectively. However, the mechanical properties of NiTiCu produced by VP in this study remain insufficient and in need of further improvement.

1. Introduction

Additive manufacturing (AM) is a process to fabricate an object from a 3D model and has become a powerful tool for prototyping, manufacturing, and product development across a wide range of fields and applications [1–6]. Using AM, it is possible to create complex, customized 3D objects with more accuracy, less waste, and in less time compared to traditional manufacturing processes [7–10]. Vat photopolymerization is an AM technology that uses a photosensitive resin to create 3D objects with high accuracy and precision. The process involves projecting ultraviolet light onto a platform to cure liquid resin layer by layer [11]. The parts produced through vat photopolymerization can be used in a variety of applications, such as automotive, medical, aerospace, and consumer products [12]. This technology is constantly evolving and being used in more and more applications.

Although vat photopolymerization was originally intended for fabricating curable resins, printing other materials such as metals [13, 14], ceramics [15], wax, and biomaterials has recently gained more attention as a way to produce highly accurate components with a fine finish [16]. In the case of metals and ceramics, the particles are mixed with resin to form printable materials. The resin is then removed by thermal debinding, and the remaining solid particles are sintered at high

temperatures.

The production and development of metal alloys for powder-based additive manufacturing have been of interest to many researchers. The ability to manufacture end-use parts with more desirable properties, lower costs, and complex geometries in which materials are selectively deposited onto predefined areas are only a few of the benefits of metal AM. Various AM technologies have been used to produce metal alloy parts based on different applications [17,18]. Powder bed fusion (PBF) is the most popular AM technology for producing metal alloys from both elemental and pre-alloyed powders; the products have excellent mechanical properties and high resolution. A wide range of alloys, such as Ti-6Al-4V [19–22], stainless steel (316 L) [23], and nickel-based superalloys [24–26] have been produced using this technique. Despite the high quality of the fabricated parts, the main drawback of the PBF technique is its high processing cost. Directed energy deposition (DED) is another exclusive AM technology for producing metal alloys (e.g., titanium [27], tool steel, CoCrMo alloy [28], et cetera). For this technique, a fully dense part with a highly controllable microstructure can be made by managing the composition of the deposited materials. However, the main limitations of this technique are poor surface roughness and resolution, restricted part geometries, and very long processing times. On the other hand, material extrusion (MEX) has recently become

^{*} Corresponding author.

E-mail address: mehrdad.mousapour@aalto.fi (M. Mousapour).

<https://doi.org/10.1016/j.addma.2023.103853>

Received 4 June 2023; Received in revised form 15 October 2023; Accepted 30 October 2023

Available online 3 November 2023

2214-8604/© 2023 The Author(s). Published by Elsevier B.V. This is an open access article under the CC BY license (<http://creativecommons.org/licenses/by/4.0/>).

Table 1
The printing parameters used for NiTiCu samples.

Sample	Powder	Solid content (wt% / vol%)	Particle size d50 (μm)	Layer	Thickness (μm)	Cure time (sec)	Cure depth (mm)	Energy dose (%)
S1	Elemental	45/24	46	First	100	1000	0.151	70
				Rest	100	200	0.134	
S2	Milled	45/22	20.4	First	100	60	0.153	
				Rest	100	20	0.138	
S3	Milled	65/42	20.4	First	100	1000	0.124	
				Rest	100	200	0.109	

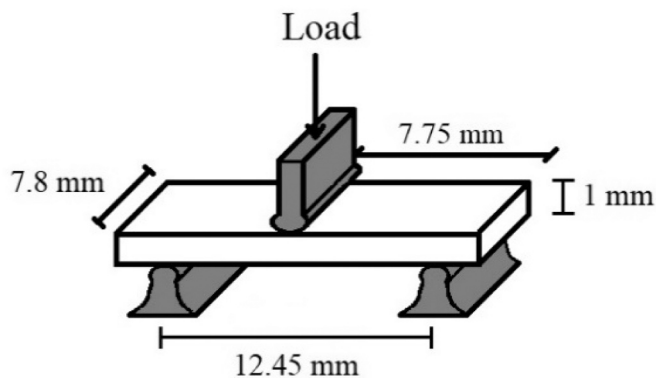


Fig. 1. A schematic of NiTiCu sample and testing setup for TRS.

more prominent for the fabrication of metal alloys due to its simplicity, affordability, and reliability; however, this technique has been associated with poor surface quality and mechanical properties. The most common alloys produced using MEX are stainless steel (316 L, 17-4PH) [29–31] and titanium (Ti-6Al-4V) [32–34], which are printed from pre-alloyed powders. Mousapour et al. [35] investigated the possibility of alloying two different metal filaments using fused filament fabrication (FFF). In the case of the vat photopolymerization technique, only a few

attempts have been made to produce metallic parts, including pure copper [36] and Inconel 718 [37]. However, limited information exists on the fabrication of metal alloys using this technique.

NiTi (nitinol) shape memory alloys are becoming more attractive in aerospace and medical applications due to their specific features such as super-elasticity and good corrosion resistance. These properties can be easily improved by adding the third element to nitinol. The addition of copper, one of the most common additives, results in narrow transformation hysteresis, improvement in fatigue properties during thermal cycling, and enhancement of thermoelasticity. However, high Cu content (> 10 at%) can reduce the fatigue life and formability of the alloy [38–40]. This work studies, for the first time, the possibility of producing and printing a uniform NiTiCu alloy from elemental and alloyed powders and compares their outcomes. Additionally, the effect of particle size and solid content on the surface quality, densification level, and mechanical properties of the final parts is assessed.

2. Experimental procedures

Commercial pure nickel (>99.9%, APS 60–70 μm), titanium (99%, APS 40–50 μm), and copper (99%, APS 40–50 μm; Nanoshel, India) powders were used to obtain Ni50Ti5Cu (at%). In addition, to compare the effect of particle size, the mixed powder was also milled for 30 h using a planetary ball mill (Fritsch Pulverisette 5/4, Germany) in an argon atmosphere. The milling test was conducted using a stainless-steel bowl and balls with a milling speed of 200 rpm. The ball-to-powder

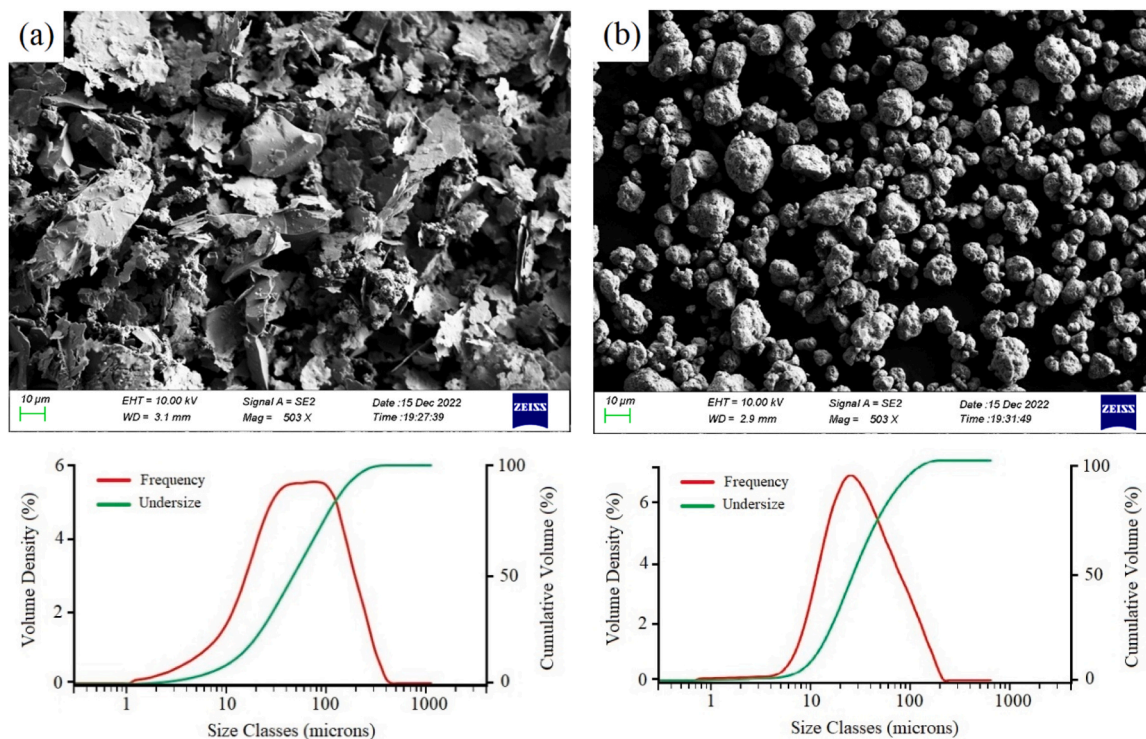


Fig. 2. The morphology and particle size distribution plot of the (a) mixed elemental and (b) milled powders.

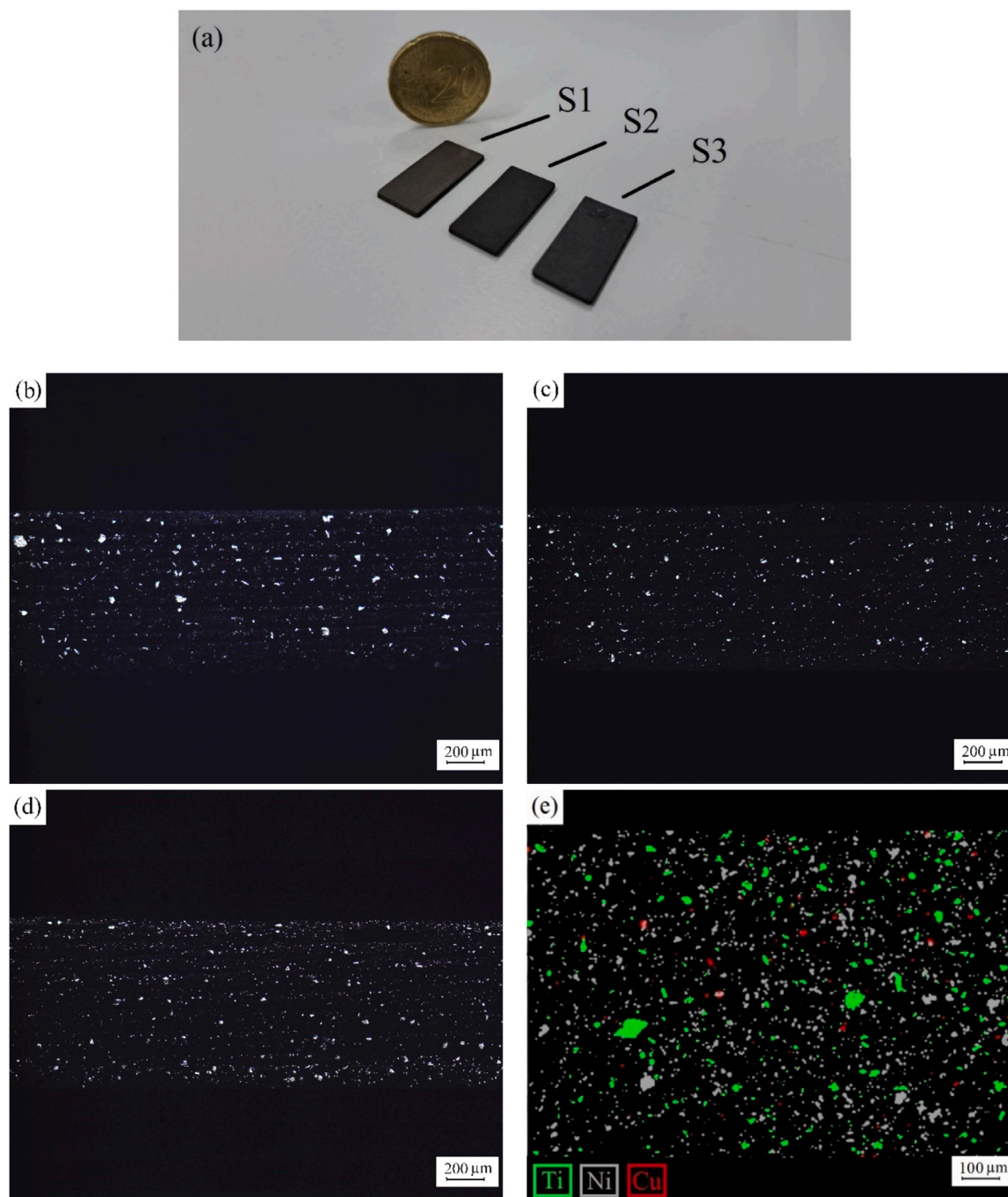


Fig. 3. (a) An image and the cross-section of (b) S1, (c) S2, and (d) S3 printed parts. (e) EDS mapping and elemental distribution from cross-section of S1 print.

weight ratio (BPR) was maintained at 10:1. The milling sequence was designed to include 10 min of milling and a 5-min idle period to prevent the powder from sticking to the bowl walls and the balls, and agglomerating during milling.

To make the materials printable, each type of powder (mixed elemental and milled) was separately mixed into a curable resin (Tethon 3D, USA) with a specific ratio. Sample 1 (S1) had a solid (mixed elemental powder) content of 45 wt% and was blended with the resin by a magnetic stirrer at 50 °C for 10 min. Similarly, 45 wt% (S2) and 65 wt% (S3) solid contents of milled powder were added to the resin to investigate the effect of the metal-resin ratio on the properties of the final part.

The rectangular cubic specimens were designed to create a sample for the transverse rupture strength (TRS) test and then printed using the

DLP technique (printer: Planmeca C5, Finland). The final size of the prints was $20 \times 10 \times 2 \pm 0.05$ mm. Since the printer used has no swiper for continuously mixing the feedstock (slurry), sedimentation happens over time, and the metal particles may settle to the bottom of the vat during a longer printing time. Based on the experiments in this study, the layers started being printed with fewer metal particles for prints over 80 min long. Therefore, thin samples (with thickness of 2 mm) were printed to avoid a solid particle gradient from top to bottom. Moreover, curing the initial layer is the most critical step in the DLP technique because sufficient adhesion to the build plate is essential. Accordingly, the first layer was exposed to UV light for longer than the remaining layers. Cure depth (time) might also change with particle size distribution and solid content. The printing parameters are given in Table 1.

The printed samples placed in an alumina boat and inserted into a

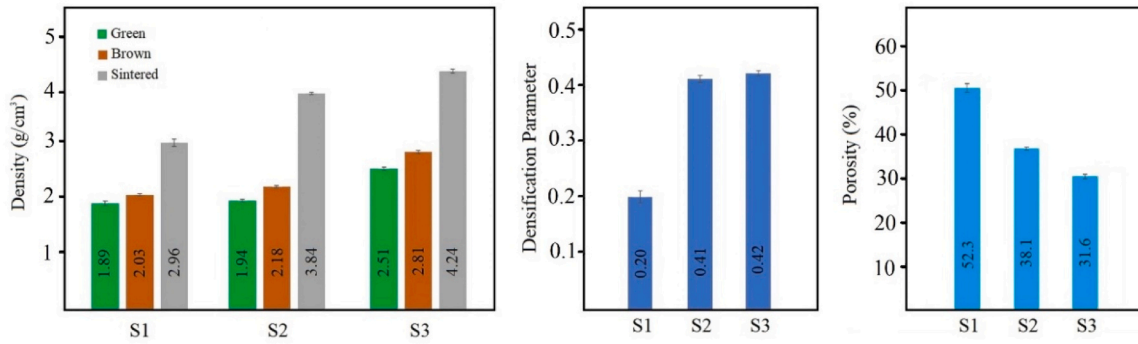


Fig. 4. The measured average densities, densification parameter, and porosity for NiTiCu.

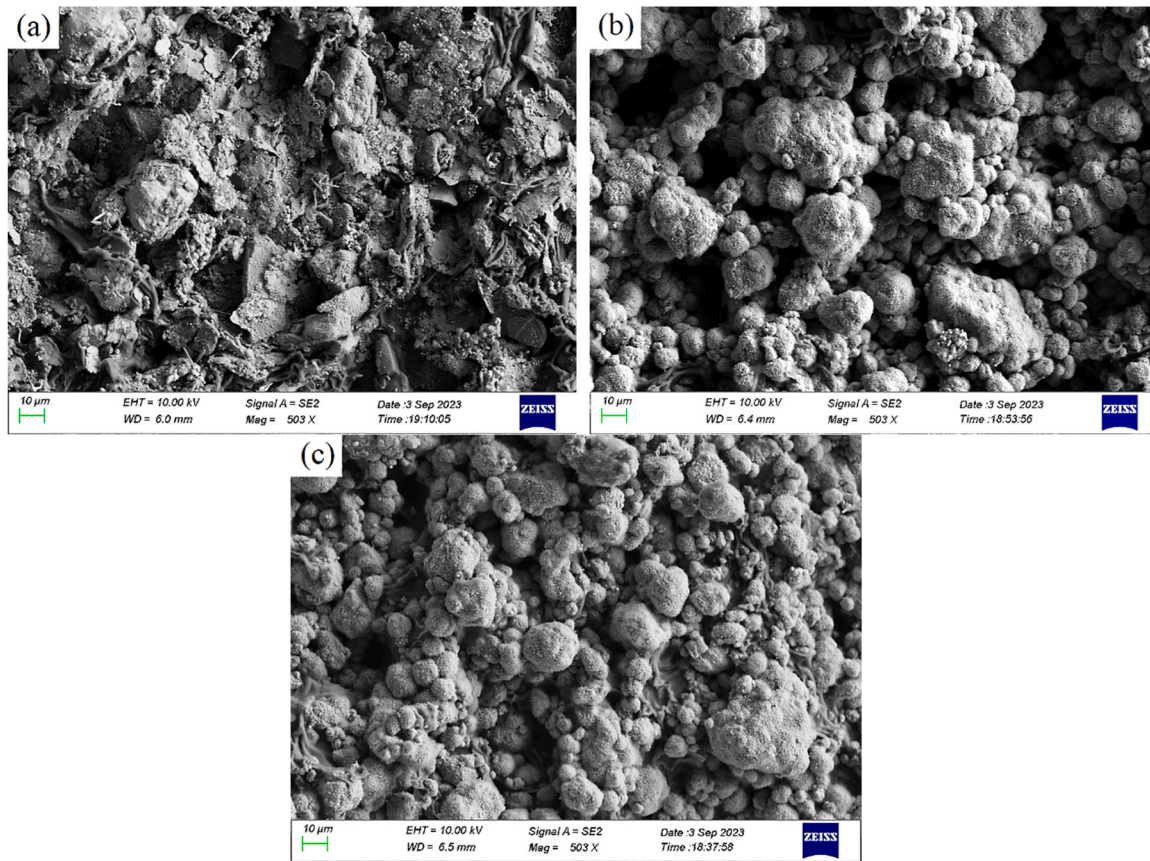


Fig. 5. Microstructure of brown (debound) samples (a) S1, (b) S2, and (c) S3.

horizontal tube furnace (Nanoe, Zsinter 2–5–17TPD2, France) for debinding and sintering processes. The temperature was measured with an external B-type thermocouple, which was connected to a logger to record the heating program. According to the manufacturer's recommendation, the debinding process was conducted in two steps: a) a ramp of 3 K/min from room temperature to 300 °C (no hold), and then b) a 1 K/min to 460 °C (held for two hours). The sample was then heated up to the target sintering temperature of 1230 °C at a rate of 3 K/min and held at this temperature for 5 h. All the samples were cooled down to room temperature in the furnace with a 3 K/min ramp. Both debinding and sintering processes were completed in an argon atmosphere with a 0.5 l/min flowing rate.

After sintering was complete, the density of each sample was measured using the Archimedes method (DIN ISO 3369) to study the densification parameter (ψ) and porosity, which are expressed as follows [41]:

$$\psi = ((\rho_{\text{sinter}} - \rho_{\text{brown}}) / (\rho_{\text{th}} - \rho_{\text{brown}})) \quad (1)$$

$$\text{Porosity (\%)} = [1 - (\rho_{\text{sinter}} / \rho_{\text{th}})] \times 100 \quad (2)$$

where ρ_{sinter} is the sintered density (g/cm^3); ρ_{brown} , the density of debound parts (g/cm^3); and ρ_{th} , the theoretical density (g/cm^3). Higher sintered density clearly results in a higher densification parameter and a lower level of porosity. The theoretical density of Ni50Ti5Cu was calculated to be 6.2 g/cm^3 . The microstructure of the samples was characterized using an optical microscope (Zeiss Axio Vert.A1, Germany) and a scanning electron microscope (SEM; Zeiss, Sigma VP, Germany) equipped with an energy dispersive spectrometer (EDS; Oxford Ultim max, UK) to analyze the shape of the pores and elemental distribution. Furthermore, X-ray diffraction (XRD; Panalytical X'Pert Pro MPD alpha1, UK) analysis was used to characterize the types of phases

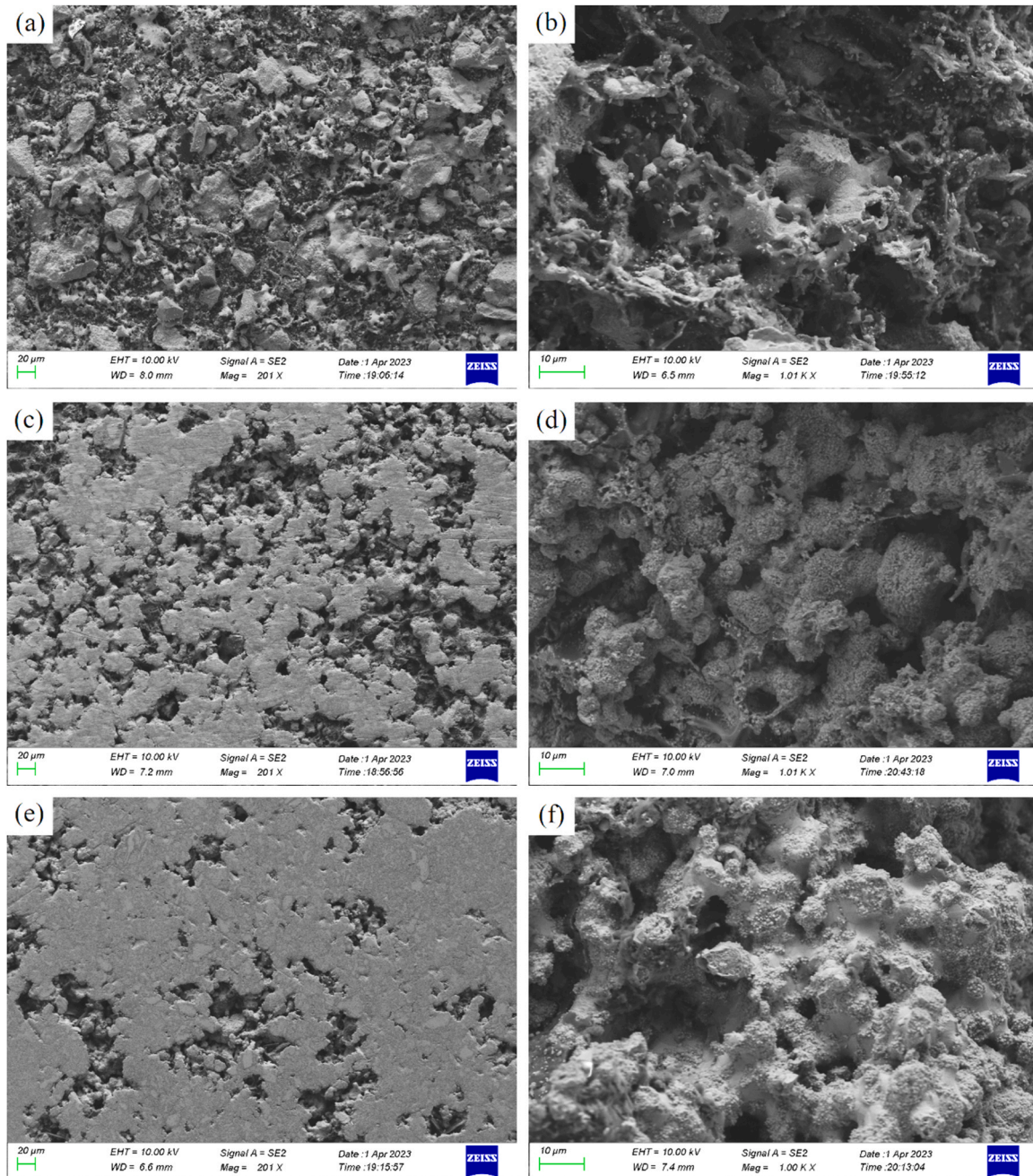


Fig. 6. Microstructure of (a, b) S1, (c, d) S2 and (e, f) S3 sintered at 1230 °C for 5 h. (Left column: the polished cross-section. Right column: the fracture surface of sintered samples.)

and compounds that might have been formed during sintering. The particle size distribution of the raw materials was studied (using Malvern Mastersizer 3000, UK) based on ISO 31320. The intensity of light scattered can be measured as a laser beam passes through the particles in dry conditions, and then the equivalent spherical diameter is calculated by the software. To compare the surface quality of the parts, the surface roughness was measured by a profilometer (Bruker Contour GT K-M, USA) for each sintered sample. To analyze the mechanical properties of the sintered samples, Vickers microhardness analysis was conducted on the cross-section of the samples using a hardness tester (Struers Duramin 40, USA) with a load of 0.490 N and a 10 s dwell time. For each specimen, the hardness was measured at five different points, and the average values were reported in the results section. Moreover, a TRS test was performed (repeated three times for each case) using a universal testing machine (MTS insight, USA) according to the ASTM standard (B

528–99) to determine the breaking strength of the samples in a transverse direction. The dimensions of the TRS samples were $15.5 \times 7.8 \times 1 \pm 0.05$ mm. The schematic of the TRS test setup is presented in Fig. 1.

3. Results and discussion

The morphology and particle size distribution plots of both mixed elemental and milled powders are depicted in Fig. 2. After 30 h of milling, the irregular-shaped particles transform into semi-spherical shapes. According to the results of particle size distribution, the mixed elemental powder has a range of 1.28 – 400 μm and a median (d_{50}) of 46 μm , while the range for the milled powder is 0.67 – 127 μm , with a d_{50} of 20.4 μm . Based on the results and SEM images, it is obvious that the particles become smaller after milling.

After mixing the powders into the resin with the prespecified ratios,

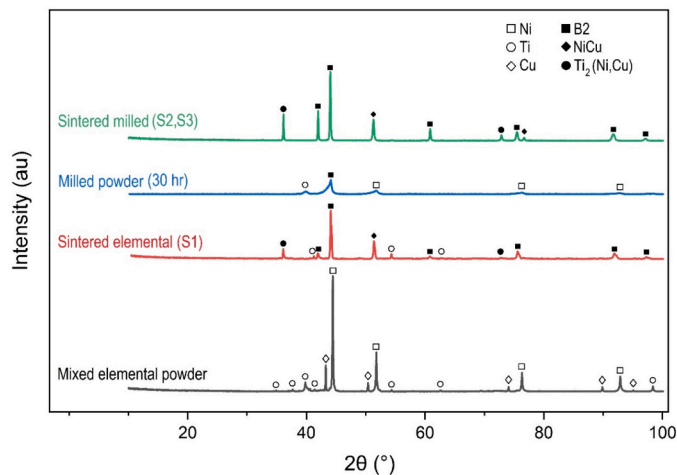


Fig. 7. XRD patterns of elemental and 30-hours-milled NiTiCu powders before and after sintering.

the specimens are printed (green parts) and then debound (brown part) to separate the metal particles from the binding material for the sintering process. Photographs of all three printed samples and the polished cross-section of the green parts are included in Fig. 3. The dark and bright areas in OM images represent resin and solid particles, respectively. These microstructures indicate that there is no solid content gradient from top to bottom, and metal particles are uniformly printed throughout the samples. Fig. 3c presents the S2 cross-section with the same solid content as S1 (Fig. 3b), but with a finer particle size, while a higher solid content is visible in S3 (Fig. 3d). Fig. 3e depicts the elemental analysis (EDS) from the cross-section of the S1 printed sample. This analysis proves that blending the elemental powders for a long time in a mixer is not necessary; this is a common step in conventional methods to achieve an acceptable distribution of particles. Instead, a reasonably distributed structure can be obtained via the vat photopolymerization technique by mixing the powders in a resin in much less time (10 min).

The average specimen densities, along with the standard deviation (SD), are measured for green, brown, and sintered parts, which are plotted in Fig. 4. The green densities of S1 and S2 are about the same due to similar solid content, while S3 has the highest value with 65 wt% solid particles. Furthermore, the measured brown densities indicate that the debound S2 with a finer particle size is denser than S1, where a larger particle size results in bigger gaps among particles. Fig. 5 presents the microstructure of the brown samples after the debinding process. The comparison of the sintered densities of three samples proves that a) **particle size** and b) **solid content** are two effective parameters that play a key role in the level of porosity. In fact, finer particle size and higher solid content enhance the average contact area among the particles, thus accelerating the diffusion mechanism. According to the measured values, a higher densification degree (parameter) is observed in finer particle sizes, while solid content has no sensible effect. However, in similar particle size, S3 with higher brown density has slightly lower porosity level than S2. Although the solid content could not exceed 65 wt% in this study due to technical limitations of the printer, the porosity in all three cases is still relatively high. However, considering all factors, particle size impacts the final porosity level more than solid content.

The microstructures of each specimen are depicted in Fig. 6. As evidenced by the polished cross-section SEM images, S3 has the highest level of density among all samples (Fig. 6e), a finding that corroborates the measured sintered density values. In contrast, the free spaces (gaps) between the elemental particles in S1, which occur due to larger particle size and lower solid content, critically restrict its contact area. Consequently, the bonds formed between the particles are narrow and weak.

Fig. 6a presents the polished cross-section of S1, where the joints are broken and particles are separated from the sample after grinding. Furthermore, pure copper particles in S1 melt at temperatures above 1085 °C, and since the copper liquid is fully soluble in solid nickel and titanium structures (transient liquid phase sintering), the formed liquid disappears during sintering. Therefore, empty spaces (gaps) remain at the sites of copper particles, increasing the number of micro-pores in the structure. In this condition, these micro-gaps hinder solid-state diffusion among the particles. The porosity is consequently not efficiently diminished, and swelling occurs [42–46]. The fracture surface of each sample is also illustrated with higher magnification for better observation of the pores' structure and the formed bonding among particles (Fig. 6b, d, f).

Fig. 7 illustrates the XRD patterns of both elemental and milled powders measured before and after sintering. Analysis of the results reveals that most of the peaks belonging to the pure elements disappear after milling, proving that mechanical alloying occurs to some extent after 30 h of milling. In fact, the position of the most intense Ni peak (44.4°) shifts to lower angles and forms the B2 phase, which represents austenite NiTiCu. This result illustrates the diffusion of Cu and Ti atoms into the nickel structure, resulting in an increase in Ni lattice parameters. Moreover, no Cu peak is observed in the milled powder pattern, indicating complete dissolution of copper in the Ni lattice (due to low copper content in the raw mixed powder). After sintering, both patterns (sintered elemental and milled) exhibit relatively similar peaks, including the B2 phase, and some precipitates such as Ti₂(Ni,Cu) and NiCu are due to the addition of copper. However, there are still some elemental peaks (Ti) in the S1 pattern, which suggests that the sample is not fully alloyed after sintering. This outcome might be caused by the larger particle size in S1, which reduces the contact areas among the particles, thus obstructing material transport. Since alloying in solid-state sintering is based on the diffusion mechanism (material transport), a higher sintering temperature or a longer time is required to obtain a fully alloyed sample.

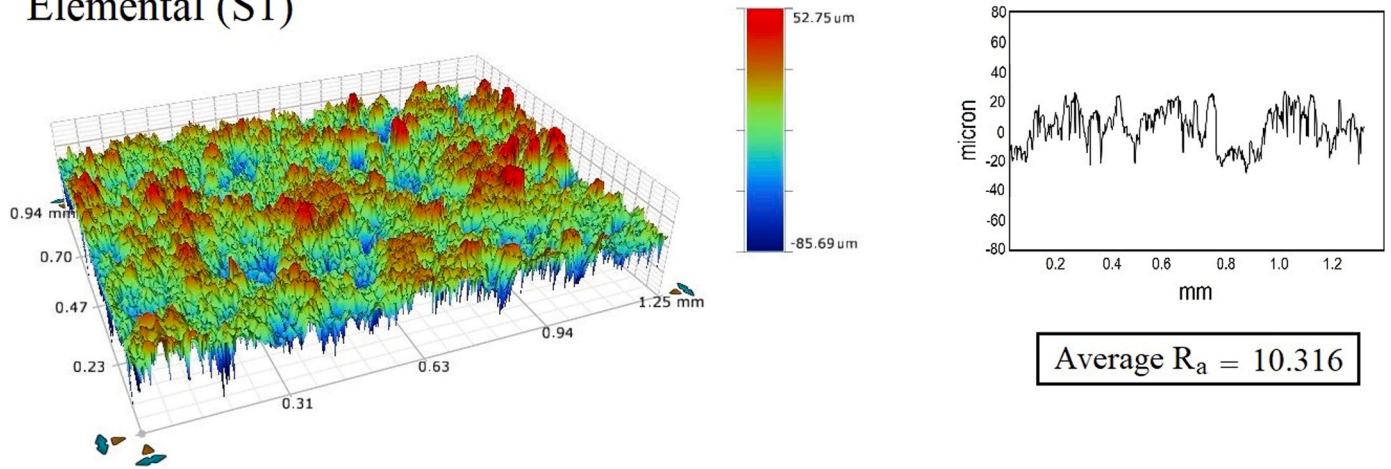
The surface roughness is determined by averaging four measurements from different areas (scanning size = 0.9 × 1.3 mm); findings are reported in Fig. 8. According to the data, S3 has the best surface quality with the lowest R_a (average roughness). 3D scans of the samples' surfaces as well as the linear models clearly reflect the difference in surface roughness among the three specimens. It seems that particle size has a major effect on the surface quality of sintered samples, such that finer particle size decreases the R_a value. Additionally, a higher solid content can improve the surface quality to some extent. In this case, the metal particles in the sample with higher solid content (S3) are more regularly arranged alongside each other than those in S2 after the debinding process. In fact, higher resin content reduces the chance of particles arranging in a more orderly manner after resin removal, due to more spaces between the particles. Consequently, S3 has a slightly better surface finish than S2. According to the literature, similar surface roughness values (average R_a = 6.22 μm) were reported by Kesavan and Velmurugan [47,48] for machined NiTi parts produced by powder metallurgy (a conventional method). This level of surface quality was obtained with the DLP technique (in this study) without post-processing.

The measured data, including SD, for TRS and hardness tests are plotted in Fig. 9. S1 has the lowest flexural strength (12.4 MPa) compared to the milled samples, while S3 has slightly higher strength than S2 (23.5 MPa and 20.5 MPa, respectively). Similar results are observed in the hardness measurements: S3 has the highest average hardness value of 461.1 HV0.05. Due to the high level of porosity in each specimen, the mechanical properties are not as desired, which is expected from VP. This technique is still extremely new in metal alloying, and further research is needed to enhance its properties.

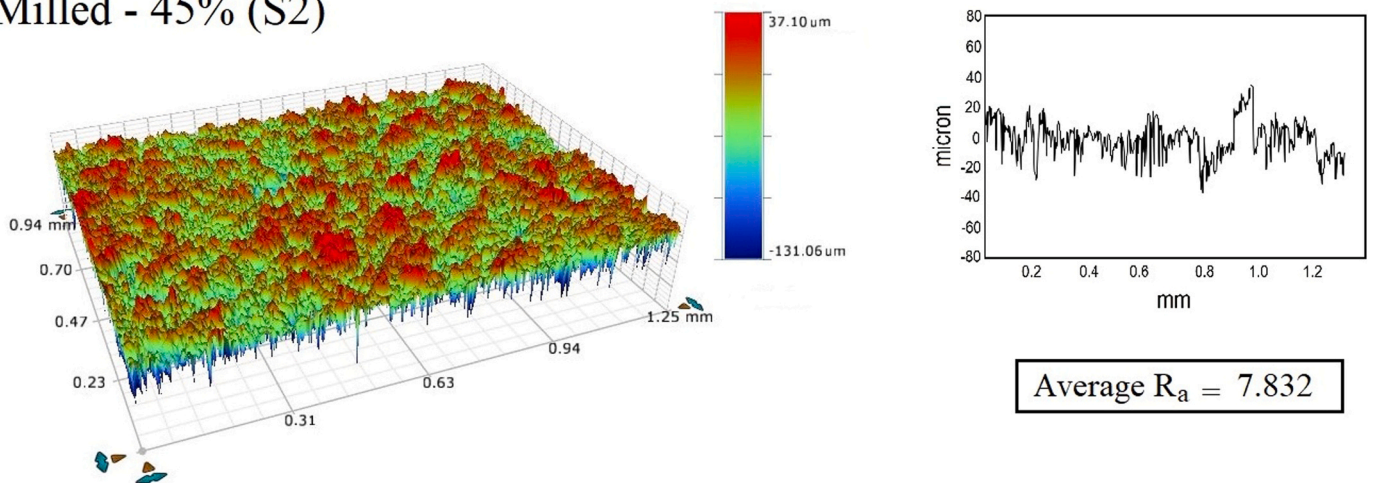
4. Conclusions

In this work, a metal alloy (NiTiCu) was successfully produced from

Elemental (S1)



Milled - 45% (S2)



Milled - 65% (S3)

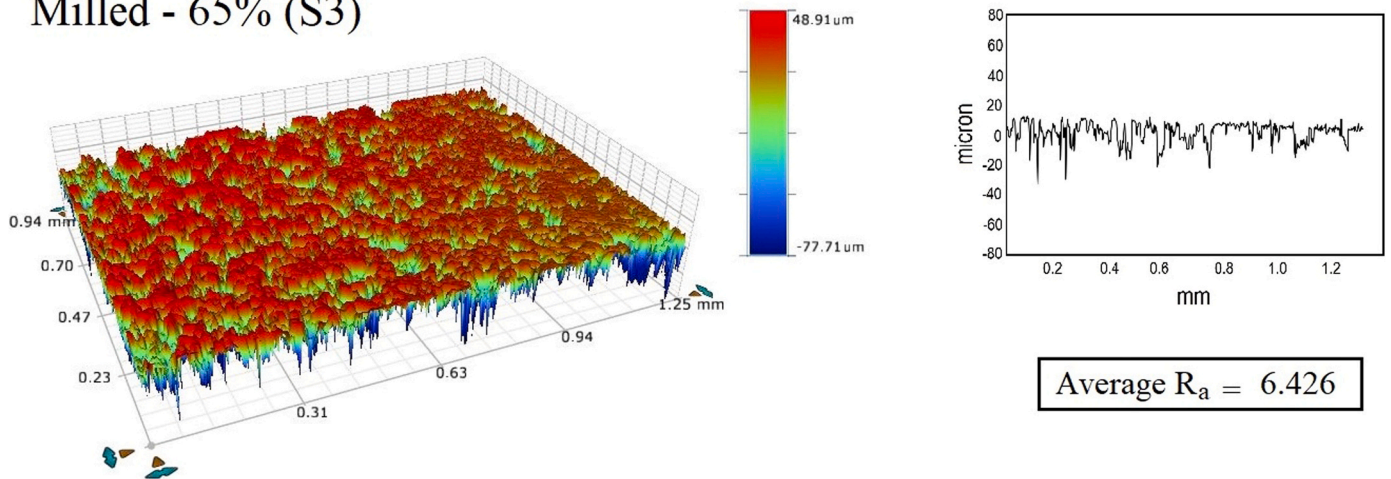


Fig. 8. 3D surface topographic, linear regression, and average surface roughness values (R_a) of sintered NiTiCu samples.

elemental and milled powders for the first time using the DLP technique, and the physical and mechanical properties of the final parts were analyzed and compared. It was hypothesized that better properties could be obtained in parts with finer particles and higher solid content (metal particles). However, according to the measured data, particle size was

more effective than solid content, especially in terms of mechanical properties. The results further indicated that it is possible to produce the metal alloy from elemental powders using the vat photopolymerization technique. However, the properties can be further improved by reducing the particle size, increasing the solid content, and using some additives

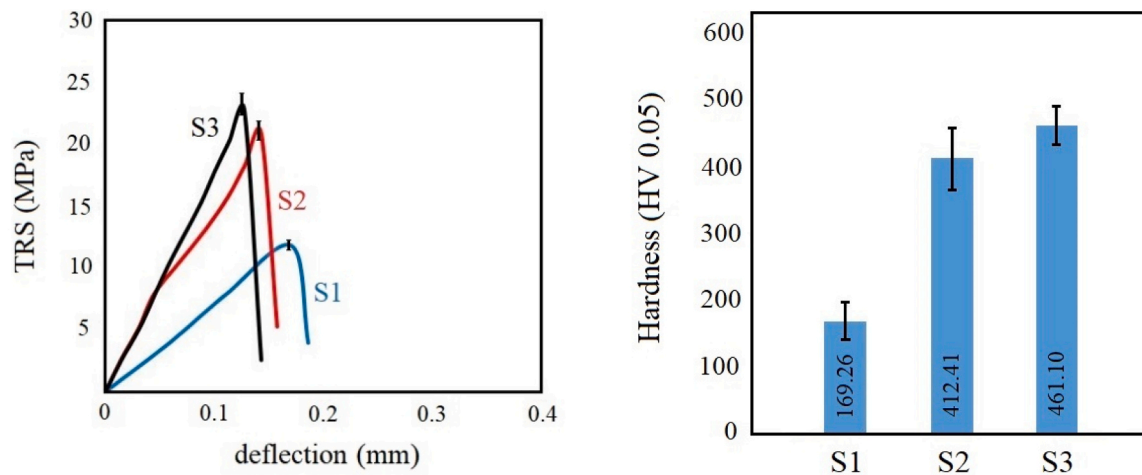


Fig. 9. The measured TRS and hardness (HV 0.05) of sintered NiTiCu samples.

to decrease the sintering temperature, which will be further investigated in future studies. The results indicate that a wide range of chemical compositions of metal alloys, as well as accepted resolutions, can be obtained using the DLP technique; it would be difficult, if not impossible, to produce parts with similar properties using conventional technologies.

CRediT authorship contribution statement

Mehrdad Mousapour: Writing – original draft, Methodology, Investigation, Formal analysis, Data curation. **Jouni Partanen:** Writing – review & editing, Methodology. **Mika Salmi:** Writing – review & editing, Supervision, Methodology, Funding acquisition.

Declaration of Competing Interest

The authors declare that they have no known competing financial interests or personal relationships that could have appeared to influence the work reported in this paper.

Data Availability

Data will be made available on request.

Acknowledgments

This work was partially supported by the JAES Foundation 285.591.

References

- [1] I. Gibson, D. Rosen, B. Stucker, *Additive Manufacturing Technologies*, Springer, New York, NY, 2014.
- [2] L. Yang, K. Hsu, B. Baughman, D. Godfrey, F. Medina, M. Menon, S. Wiener, *Additive Manufacturing of Metals: The Technology, Materials, Design, and Production*, Springer International Publishing, 2017.
- [3] M.A.G. Calle, M. Salmi, L.M. Mazzariol, M. Alves, P.C. Kujala, Additive manufacturing of miniature marine structures for crashworthiness verification: Scaling technique and experimental tests, *Mar. Struct.* 72 (2020), 102764.
- [4] J.S. Akmal, M. Salmi, B. Hemming, L. Teir, A. Suomalainen, M. Kortensniemi, J. Partanen, A. Lassila, Cumulative inaccuracies in implementation of additive manufacturing through medical imaging, 3D thresholding, and 3D modeling: a case study for an end-use implant, *Appl. Sci.* 10 (8) (2020) 2968.
- [5] M.A.G. Calle, M. Salmi, L.M. Mazzariol, P.C. Kujala, Miniature reproduction of raking tests on marine structure: similarity technique and experiment, *Eng. Struct.* 212 (2020), 110527.
- [6] J.S. Akmal, M. Salmi, A. Makitie, R. Björkstrand, J. Partanen, Implementation of industrial additive manufacturing: intelligent implants and drug delivery systems, *J. Funct. Biomater.* 9 (3) (2018).
- [7] M. Salmi, J. Tuomi, R. Sirkkänen, T. Ingman, A. Makitie, Rapid tooling method for soft customized removable oral appliances, *Open Dent. J.* 6 (1) (2012) 85–89.
- [8] N. Kretzschmar, S. Chekurov, M. Salmi, J. Tuomi, Evaluating the readiness level of additively manufactured digital spare parts: an industrial perspective, *Appl. Sci.* 8 (10) (2018).
- [9] S. Chekurov, S. Metsa-Kortelainen, M. Salmi, I. Roda, A. Jussila, The perceived value of additively manufactured digital spare parts in industry: an empirical investigation, *Int. J. Prod. Econ.* 205 (2018) 87–97.
- [10] M. Salmi, I.F. Ituarte, S. Chekurov, E. Huutilainen, Effect of build orientation in 3D printing production for material extrusion, material jetting, binder jetting, sheet object lamination, vat photopolymerization, and powder bed fusion, *Int. J. Collab. Enterp.* 5 (3/4) (2016) 218–231.
- [11] M. Pagac, J. Hajnys, Q.P. Ma, L. Jancar, J. Jansa, P. Stefek, J. Mesicek, A review of vat photopolymerization technology: materials, applications, challenges, and future trends of 3D printing, *J. Polym.* 13 (4) (2021).
- [12] N. Guo, M.C. Leu, Additive manufacturing: technology, applications, and research needs, *Front Mech. Eng.* 8 (2013) 215–243.
- [13] A.M. Clarinval, R. Carrus, T. Dormal, Q. Soyeur, Fabrication of stainless steel and ceramic parts with the Optoform process, *Adv. Virtual Rapid. Manuf.* (2007) 415–418.
- [14] S. Kumar, J.P. Kruth, Composites by rapid prototyping technology, *Mater. Des.* 31 (2) (2010) 850–856.
- [15] O. Dufaud, S. Corbel, Stereolithography of PZT ceramic suspensions, *Rapid Prototyp. J.* 8 (2) (2002) 83–90.
- [16] F. Zhang, L. Zhu, Z. Li, S. Wang, J. Shi, W. Tang, N. Li, J. Yang, The recent development of vat photopolymerization: a review, *Addit. Manuf.* 48 (2021).
- [17] A. Bandyopadhyay, B. Heer, Additive manufacturing of multi-material structures, *Mater. Sci. Eng. R.* 129 (2018) 1–16.
- [18] M. Vaezi, S. Chianrabutra, B. Mellor, S. Yang, Multiple material additive manufacturing - part 1: a review, *Virtual Phys. Prototyp.* 8 (1) (2013) 19–50.
- [19] M. Mazur, M. Leary, M. McMillan, S. Sun, D. Shidid, M. Brandt, Mechanical properties of Ti6Al4V and AlSi12Mg lattice structures manufactured by Selective Laser Melting (SLM), *Laser Addit. Manuf.* (2017) 119–161.
- [20] Q. Liu, Y. Wang, H. Zheng, K. Tang, L. Ding, H. Li, S. Gong, Microstructure and mechanical properties of LMD–SLM hybrid forming Ti6Al4V alloy, *Mater. Sci. Eng. A.* 660 (2016) 24–33.
- [21] T. Vilaro, C. Colin, J.D. Bartout, As-fabricated and heat-treated microstructures of the Ti-6Al-4V alloy processed by selective laser melting, *Metall. Mater. Trans. A.* 42 (10) (2011) 3190–3199.
- [22] H. Galarraga, D.A. Lados, R.R. Dehoff, M.M. Kirka, P. Nandwana, Effects of the microstructure and porosity on properties of Ti-6Al-4V ELI alloy fabricated by electron beam melting (EBM), *Addit. Manuf.* 10 (2016) 47–57.
- [23] T. Puttonen, S. Chekurov, J. Kuva, R. Björkstrand, J. Partanen, M. Salmi, Influence of feature size and shape on corrosion of 316L lattice structures fabricated by laser powder bed fusion, *Addit. Manuf.* 61 (2023).
- [24] H.E. Helmer, C. Körner, R.F. Singer, Additive manufacturing of nickel-based superalloy Inconel 718 by selective electron beam melting: processing window and microstructure, *J. Mater. Res.* 29 (17) (2014) 1987–1996.
- [25] W.J. Sames, K.A. Unocic, R.R. Dehoff, T. Lolla, S.S. Babu, Thermal effects on microstructural heterogeneity of inconel 718 materials fabricated by electron beam melting, *J. Mater. Res.* 29 (17) (2014) 1920–1930.
- [26] Y. Zhang, J. Zhang, Sintering phenomena and mechanical strength of nickel based materials in direct metal laser sintering process—a molecular dynamics study, *J. Mater. Res.* 31 (15) (2016) 2233–2243.
- [27] K.I. Schwendner, R. Banerjee, P.C. Collins, C.A. Brice, H.L. Fraser, Direct laser deposition of alloys from elemental powder blends, *Scr. Mater.* 45 (10) (2001) 1123–1129.
- [28] B.V. Krishna, W. Xue, S. Bose, A. Bandyopadhyay, Functionally graded Co–Cr–Mo coating on Ti–6Al–4V alloy structures, *Acta Biomater.* 4 (3) (2008) 697–706.

- [29] I. Ait-Mansour, N. Kretschmar, S. Chekurov, M. Salmi, J. Rech, Design-dependent shrinkage compensation modeling and mechanical property targeting of metal FFF, *Prog. Addit. Manuf.* 5 (2020) 51–57.
- [30] Y. Thompson, J. Gonzalez-Gutierrez, C. Kukla, P. Felfer, Fused filament fabrication, debinding, and sintering as a low-cost additive manufacturing method for 316L stainless steel, *Addit. Manuf.* 30 (2019).
- [31] J. Gonzalez-Gutierrez, D. Godec, R. Gurán, M. Spoerk, C. Kukla, C. Holzer, 3D printing conditions determination for feedstock used in fused filament fabrication (FFF) of 17-4PH stainless steel parts, *Metalurgija* 57 (1–2) (2018) 117–120.
- [32] Y. Zhang, S. Bai, M. Riede, E. Garratt, A. Roch, A comprehensive study on fused filament fabrication of Ti-6Al-4V structures, *Addit. Manuf.* 34 (2020).
- [33] P. Singh, V.K. Balla, A. Tofangchi, S.V. Atre, K.H. Kate, Printability studies of Ti-6Al-4V by metal fused filament fabrication (MF3), *Int. J. Refract. Hard Met.* 91 (2020).
- [34] P. Singh, V.K. Balla, S.V. Atre, R.M. German, K.H. Kate, Factors affecting properties of Ti-6Al-4V alloy additive manufactured by metal fused filament fabrication, *Powder Technol.* 386 (2021) 9–19.
- [35] M. Mousapour, M. Salmi, L. Klemettinen, J. Partanen, Feasibility study of producing multi-metal parts by Fused Filament Fabrication (FFF) technique, *J. Manuf. Process.* 67 (2021) 438–446.
- [36] M. Roumanie, C. Flassayer, A. Resch, L. Cortella, R. Laucourmet, Influence of debinding and sintering conditions on the composition and thermal conductivity of copper parts printed from highly loaded photocurable formulations, *SN Appl. Sci.* 3 (2021) 1–11.
- [37] Y. Zhang, S. Li, X. Liu, X. Li, W. Duan, L. Li, B. Liu, G. Wang, Additive manufacturing and characterization of microstructure evolution of inconel 718 superalloy produced by vat photopolymerization, *Addit. Manuf.* 61 (2023), 103367.
- [38] K. Lin, S. Wu, Multi-stage transformation in annealed Ni-rich Ti49Ni41Cu10 shape memory alloy, *Intermetallics* 18 (1) (2010) 87–91.
- [39] A. Etaati, K. Dehghani, Microstructural evolution of NiTi47.7Cu6.3 alloy during hot deformation, *J. Mater. Sci. Technol.* 27 (10) (2011) 951–960.
- [40] A. Morone, Pulsed laser deposition of the NiTiCu thin film alloy, *Appl. Surf. Sci.* 253 (19) (2007) 8242–8244.
- [41] R.M. German, *Liquid phase sintering*, Springer, New York, NY, 1985.
- [42] R.M. German, *Sintering Theory and Practice*, John Wiley & Sons, Inc, New York, NY, 1996.
- [43] M. Mousapour, M. Azadbeh, H. Danninger, Effect of compacting pressure on shape retention during supersolidus liquid phase sintering of Cu base alloys, *Powder Metall.* 60 (5) (2017) 393–403.
- [44] S. Ghasemi, M. Azadbeh, M. Mousapour, A. Mohammadzadeh, H. Danninger, N. Salimi, The role of pore evolution during supersolidus liquid phase sintering of prealloyed brass powder, *Powder Metall.* 63 (3) (2020) 187–196.
- [45] M. Mousapour, M. Azadbeh, H. Danninger, Feasibility study of ‘elephant foot’ phenomenon during liquid phase sintering of systems with volatile components, *Powder Metall.* 59 (5) (2016) 321–328.
- [46] M. Mousapour, M. Azadbeh, A. Mohammadzadeh, H. Danninger, On the deflection behavior of prealloyed alpha brass during sintering: in-situ bending technique and modeling, *Powder Metall.* 63 (2) (2020) 134–141.
- [47] J. Kesavan, C. Velmurugan, V. Senthilkumar, S. Dinesh, Optimization of WEDM parameters on surface integrity characteristics of NiTi shape memory alloy, *Mater. Today Proc.* 43 (2021) 183–190.
- [48] C. Velmurugan, V. Senthilkumar, S. Dinesh, D.A. kirubakaran, Artificial neural network prediction of wire electrical discharge machining properties on sintered porous NiTi shape memory alloy, *Mater. Today Proc.* 5 (2) (2018) 8382–8390.